Space Telescope Imaging Spectrograph Detectors and Ultraviolet Signal-to-Noise[a] Capabilities

M. E. Kaiser[b,c,d] B. E. Woodgate[b,d] R. A. Kimble[b,d] C. W. Bowers[b,d] S. B. Kraemer[b,e]

V. S. Argabright[f] P. A. Driggers[f] D.J. Lindler[g] R. C. Bohlin[h]

C. N. Van Houten[f] R. L. Bybee[f] A. W. Delamere[f] D. A. Dorn[f] A. C. Danks[b,i]

C. L. Joseph[b,j] J. G. Timothy[b,k] T. R. Gull[b,d] T. L. Beck[g] M. Blouke[l] L. W. Brown[d]

M. D. Brumfield[d] M. Clampin[h] D. A. Content[d] L. D. Feinberg[d] W. B. Fowler[d]

P. Goudfrooij[h] R. J. Hill[i] R. Reed[m] C. Standley[i,d,n] J. J. Yagelowich[d]

[c] Department of Physics and Astronomy,
The Johns Hopkins University, Baltimore, MD 21218
[d]Goddard Space Flight Center, Code 680, Greenbelt, MD 21077
[e]Catholic University of America, Washington, DC 20064
[f]Ball Aerospace and Technologies Corporation, Boulder CO 80301
[g]Advanced Computer Concepts, Inc, Potomac, MD 20854
[h]Space Telescope Science Institute, 3700 San Martin Drive,
Baltimore, MD 21218
[i]Raytheon/STX
[j]Physics Department, Rutgers University, New Brunswick, NJ 08903
[k]Pegasus Glassworks, Inc., Sturbridge, MA 01566
[l]SITe Corporation, Beaverton, OR 97006
[m]National Optical Astronomy Observatories,
Kitt Peak National Observatory, Tucson, AZ 85726
[n]Adaptive Optics Associates, Cambridge, MA 02140

ABSTRACT

The Space Telescope Imaging Spectrograph (STIS) was designed as a versatile spectrograph capable of maintaining or exceeding the spectroscopic capabilities of both the Goddard High Resolution Spectrograph (GHRS) and the Faint Object Spectrograph (FOS) over the broad bandpass extending from the ultraviolet (115 nm) through the visible (1 μm). STIS achieves performance gains over the aforementioned first generation Hubble Space Telescope (HST) instruments primarily through the use of large (1024×1024) areal detectors in both the ultraviolet and visible regions of the spectrum. Simultaneous spatial and spectral coverage is provided through long slit or slitless spectroscopy of extended sources. A substantial multiplexing advantage is achieved for ultraviolet echelle spectroscopy. This paper will review the detector design and in-flight performance. Attention will be focussed on the key issue of S/N performance. Spectra obtained during the first few months of operation, illustrate that high signal-to-noise spectra can be obtained while exploiting STIS's multiplexing advantage. From analysis of a single spectrum of GD153, with counting statistics of $\sim$165, a S/N of $\sim$130 is achieved per spectral resolution element in the FUV. In the NUV a single spectrum of GRW+70D5824, with counting statistics of $\sim$200, yields a S/N of $\sim$150 per spectral resolution element. An even higher S/N capability is illustrated through the use of the fixed pattern (FP) split slits in the medium resolution echelle modes where observations of BD28D42 yield a signal-to-noise of $\sim$250 and $\sim$350 per spectral resolution element in the FUV and NUV respectively.

Correspondence should be referred to M. E. Kaiser at kaiser@pha.jhu.edu

[a]Based on Observations with the NASA/ESA *Hubble Space Telescope*, obtained at the Space Telescope Science Institute, which is operated by the Association of Universities for Research in Astronomy, Inc. (AURA), under NASA contract NAS5-26555.

[b] Co-Investigator, STIS Investigation Definition Team

Keywords: HST, STIS, instruments, detectors, CCD, MAMA, ultraviolet, spectroscopy, signal-to-noise

1. INTRODUCTION

The Space Telescope Imaging Spectrograph (STIS) is a second generation Hubble Space Telescope (HST) instrument which was designed as a versatile imaging spectrograph capable of providing spatially extended wavelength coverage from the far ultraviolet (115 nm) to the near-infrared (1 μm).[1] Spectrograph versatility, provided by the large complement of slit/grating/detector combinations, hinges upon STIS's two dimensional detectors in both the ultraviolet and the visible. The large advances provided by STIS in comparison with the first generation HST spectrographs, the Goddard High-Resolution Spectrograph (GHRS) and the Faint Object Spectrograph (FOS), stem from the use of two dimensional imaging detectors. In both the visible and the ultraviolet, STIS provides simultaneous spectral and spatial coverage with long slit or slitless spectroscopy of extended sources. In addition, a substantial multiplexing advantage is provided by using large areal detectors for echelle spectroscopy in the ultraviolet. STIS echelle modes offer 20-35 times greater simultaneous wavelength coverage than corresponding GHRS modes.

Coverage of this extensive bandpass is accomplished through the use of three detectors. In the far ultraviolet a 1024×1024 element Multi Anode Microchannel Array (MAMA) detector with a CsI photocathode provides coverage from 115-170 nm. The near ultraviolet detector is also a 1024×1024 MAMA detector, but with a Cs_2Te photocathode providing coverage from 115 to 310 nm, where 165-310 nm is the primary bandpass for this detector. Both photon counting MAMA detectors have 25×25 μm pixels with $\sim$0.025 arcsec pixel^{-1}, no read noise, and visible light rejection. In the visible (305 nm - 1μm), STIS employs a 1024×1024 pixel CCD providing a 50 arcsec field-of-view in the spatial direction.

In addition to the gains realized by using large areal detectors versus the linear arrays of the first generation instruments, STIS also benefits from advances in CCD technology since the selection of the WFPC2 detectors. STIS provides higher sensitivity UV imaging than WFPC2 through the use of a MAMA detector which has higher quantum efficiency (QE), visible light rejection and non-existent read noise compared to the WFPC2 CCD which requires use of a Woods filter for visible light rejection. The throughput of the combined WFPC2 CCD filter system is $<$2% in the FUV[2] compared to 18% throughput for the FUV MAMA at the peak of the Woods filter bandpass.

Despite the clear advantage in selecting the MAMA detectors for their aforementioned performance characteristics there was some concern over their long term pixel-to-pixel stability. This concern was driven in part by the excellent heritage of GHRS for producing high signal-to-noise spectra. Now that STIS would be replacing GHRS as the high resolution spectrograph aboard HST, at a minimum it needed to meet its specification of a signal-to-noise of 100:1 per spectral resolution element (2×2 pixels) to fill the vacancy for high-resolution, high signal-to-noise UV spectroscopy. It was hoped that the detectors would perform far better than this. However, the use of the UV MAMAs in STIS is the first use of this detector technology as a long term astronomical imager aboard a space platform and one of the first uses of any microchannel-plate based UV detectors in a high signal-to-noise longterm application.

Flat field images were acquired during ground-based calibration of the instrument. A few, non-optimal, flat field images have been acquired in flight; a more optimal set is scheduled for near term acquisition. During the Servicing Mission Orbital Verification (SMOV) program immediately after launch, stellar spectra were acquired which could be used as a signal-to-noise testbed in addition to the primary function of the data. Since signal-to-noise characterization is not the primary purpose of these spectra, single spectra do not have the counting statistics required to test the STIS signal-to-noise capability at levels much greater than 100:1. Use of the combined ground and flight flat field to calibrate the FUV data yields a signal-to-noise of $\sim$130 per spectral resolution element for a single point source spectrum of GD153. Using the ground based NUV flat field, a single point source spectrum of GRW+70D58 has a signal-to-noise of $\sim$150 per spectral resolution element.[3,4] When observing in the echelle modes, on-board Doppler compensation smooths the detector responsivity. In this case, a S/N of $\sim$250 in the FUV and $\sim$350 in the NUV[3] per spectral resolution element have been achieved by acquiring multiple spectra of BD28D42 with the fixed pattern (FP) split slits which further smooth the detector responsivity by displacing the individual spectra solely in the spectral direction. Consequently, the STIS MAMA detectors have been proven to provide not only high throughput, but also high signal-to-noise spectra.

Thorough reviews of the STIS design and in-flight performance can be found in Woodgate et al.[1] and Kimble et al.[5]

2. DETECTOR DESIGN

STIS has made a great effort to avoid single point failures in its design and operation. This philosophy extends to the selection and operation of its detectors. The Cs_2Te NUV MAMA detector is capable of providing back-up coverage for the FUV MAMA. The selection of a CCD for the visible required that the device be capable of providing spectral coverage from 180-310 nm to provide back-up coverage for the NUV MAMA. This necessitated both a development effort to improve the UV sensitivity and meticulous attention to ensure that the capability was maintained. In fact, the CCD QE between ~250 - 310 nm is higher than that of the Cs_2Te photocathode in the NUV MAMA, thus for some applications in this spectral regime the CCD will be the detector of choice. There is no backup detector for the CCD. However, the device design and operation provides a measure of redundancy and ensures that no single electronics failure will result in the loss of the entire CCD field.[6]

2.1. MAMA Detectors

Selection of the MAMA detectors for STIS in the ultraviolet hinged upon several performance advantages. MAMA detectors are a photoemissive, photon counting detector. Consequently, there is no read noise associated with the detected signal as there would be for photoconductive devices such as a CCD. This, coupled with the low background of these detectors, implies that for an equivalent QE fainter sources can be observed with the MAMA detectors. In addition, the photocathodes used by these detectors are solar blind. At 400 nm the QE is 1.5×10^{-10} and 2.7×10^{-4} for the FUV and NUV MAMA detector respectively. Detectors, such as the CCD, whose peak response is in the visible depend upon filters for visible light rejection. Typically a Woods filter is used. Unfortunately these filters have a low peak transmission and have not yet been proven stable under long term operating conditions. The combination of low background, high QE, and visible light rejection is critical for UV astronomy where the sources, in general, are faint and can be dominated by the visible region of their spectra.

A further advantage of the MAMA detectors is that they can operate at ambient temperatures. Unlike the CCD, they do not require cooling for astronomical operations. Cooled detector operations are a serious concern in the ultraviolet due to the adsorption of contaminants which can be photopolymerized by ultraviolet photons resulting in a rapidly decreasing efficiency.

The MAMA detectors provide high spatial resolution (0.05 arcsec) images across the entire 1024×1024 element array. The digital readout system provides physically distinct anode elements for the individual pixels of the array, geometrically stable imaging, and a high global dynamic range.[1]

The MAMA detector system consists of a MgF_2 entrance window which is indium sealed to an evacuated body containing the photocathode, a curved MCP (C-plate), and an anode array (Figure 1). Photons entering the detector are converted to electrons at the photocathode and accelerated into the 12μm pores of the C-plate. The C-plate has ~2000 V across its faces to drive the electrons through the plate. The secondary emitting properties of the pore surfaces produce a charge cloud of 7×10^5 electrons at the plate exit. The anode array is placed in proximity focus to minimize the dispersion of the charge cloud. The STIS C-plate achieves a higher instantaneous local count rate without altering the gain and ultimately the QE than multi-plate MCP designs such as chevrons and z-stacks. Furthermore, the lower charge extracted in each pulse increases the total number of counts that may be accommodated in the detector's lifetime. And the C shape inhibits the migration of ions back through the plate to the photocathode. A more complete discussion of the STIS MAMA detectors can be found in Woodgate et al.,[1] Timothy et al.,[7] and Joseph et al.[8]

While the FUV and NUV MAMA share the same overall design there are a few design differences, all but one of which are dependent upon the composition and hence location of the photocathode. The entrance window of the FUV MAMA is tilted by 8.5° degrees to prevent chromatic aberration in the FUV imaging mode. The inside surface of the MgF_2 window is coated with a 90% transmissive chrome layer to mitigate any dielectric charging that would cause non-uniformity in the repeller electric field. A field electrode, the repeller, is provided to force any photoelectrons produced by the MCP web ino the C-plate pores. In addition, the CsI photocathode is deposited directly on the MCP. In contrast, the NUV MAMA utilizes a semi-transparent Cs_2Te photocathode. Since the compatability of this material with the MCP surface has not been demonstrated in the laboratory, the photocathode is deposited directly on the interior surface of the NUV MAMA entrance window. The MCP is in proximity focus to the photocathode to minimize the transverse trajectory of any photoelectrons. In all other respects, the two designs are identical.

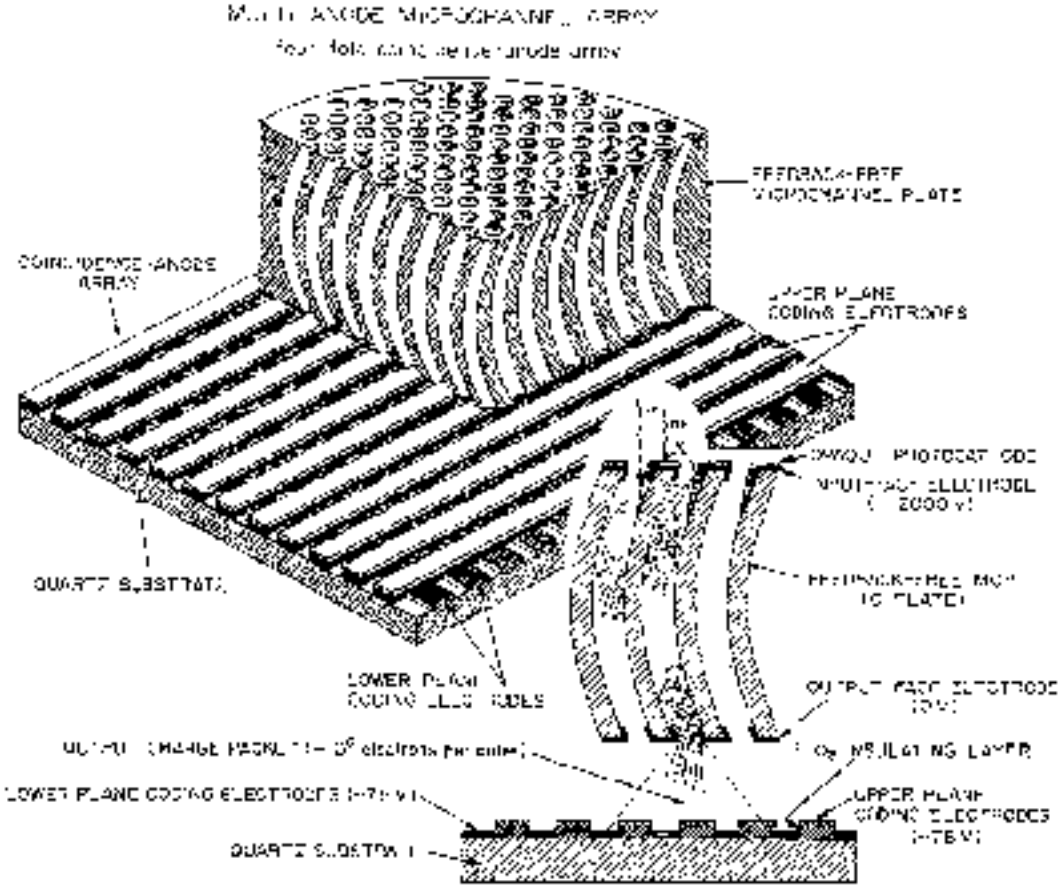

Figure 1: MAMA Detector MCP and Anode Array Schematic

2.2. CCD Detectors

For the wavelength region from 305 nm to 1μm, the CCD was the obvious detector choice. Contemporary CCDs exhibit relatively high quantum efficiency, low read noise, low dark current, good charge transfer efficiency (CTE), and have relatively few cosmetic defects. The STIS requirement that the CCD be capable of functioning as a back-up detector for the NUV MAMA from 180 - 310 nm motivated the selection of a thinned backside illuminated device. This requirement also necessitated a development effort by Scientific Imaging Technologies (SITe) to develop a UV enhancement process for the STIS CCD. The recipe chosen by STIS is one which achieved, at the time of detector selection, the highest QE while being least responsive to UV flooding. In a hard vacuum environment no quantum efficiency hysteresis is seen. Exposing localized regions of the STIS CCD to intense UV flood in vacuum, shows no detectable change in efficiency to better thant 1% precision in subsequent flat field exposures.[6]

There is a tendency for the UV-enhancement process to produce devices with an elevated dark current relative to their non-UV-enhanced counterparts. The higher background devices have a dark current level of 6 e^{-}pixel^{-1}hour^{-1} at the nominal in-flight operating temperature of -83°C.[5]

Housing design (Figures 2 and 3) was motivated by the STIS requirement to maintain the CCD's UV sensitivity down to 180 nm. Use of cold detectors in the ultraviolet pose an efficiency risk due to the preferential adsorption of contaminants, which are subsequently photpolymerized by UV photons, onto the cold surface. Design considerations led WFPC2 to employ a cold MgF_2 field flattener/window in front of each of its CCDs. Operating with a cold detector window necessitated launching an extremely clean instrument and rigorous monthly decontaminations to restore and preserve UV throughput.

Alternatively, STIS chose to operate with a cold CCD in an evacuated metal and ceramic sealed housing maintained at ambient temperature. This decision required meticulous cleaning and baking of the sealed components to

ensure that outgassing would not degrade the vacuum over time, with contaminants preferentially adsorbing onto the cold CCD. Four Zr-V-Fe getters were employed to provide long term pumping against residual outgassing products. The only mechanical coupling between the CCD and the ambient environment is via the fine signal and control wires[8] (Figure 2).

Susceptibility of the CCD to radiation damage in flight, primarily from trapped high energy photons in the South Atlantic Anomaly (SAA) which degrade the CTE and dark current performance,[9,10] motivated the following design features. The CCD housing is constructed from 1 cm thick molybdenum to shield against these high energy protons. Inverted MPP operation of the CCD is employed to reduce the sensitvity of the CCD to ionization damage by minimizing the surface state contribution to dark current. Minichannel implants were implemented to reduce the exposure to radiation induced traps in the crystal lattice by confining low signal level charge packets to a physicallly smaller "notched" potential well. In addition, CCD clock voltages can be re-optimized as damage accumulates. The spectrum can be redirected on the CCD format to minimize the number of parallel transfers and thus minimize the impact of CTE degradataion. And, four amplifier readout can be employed to minimize pixel transfers and hence minimize the impact of CTE degradation.[6]

Since there is no back-up detector for the CCD, the CCD biases, clocks, and outputs were carefully segregated so that no single point failure would result in the loss of more than on half of the detector. In the spectroscopic mode, full wavelength coverage is preserved for any such failure; half of the spatial coverage can be lost.

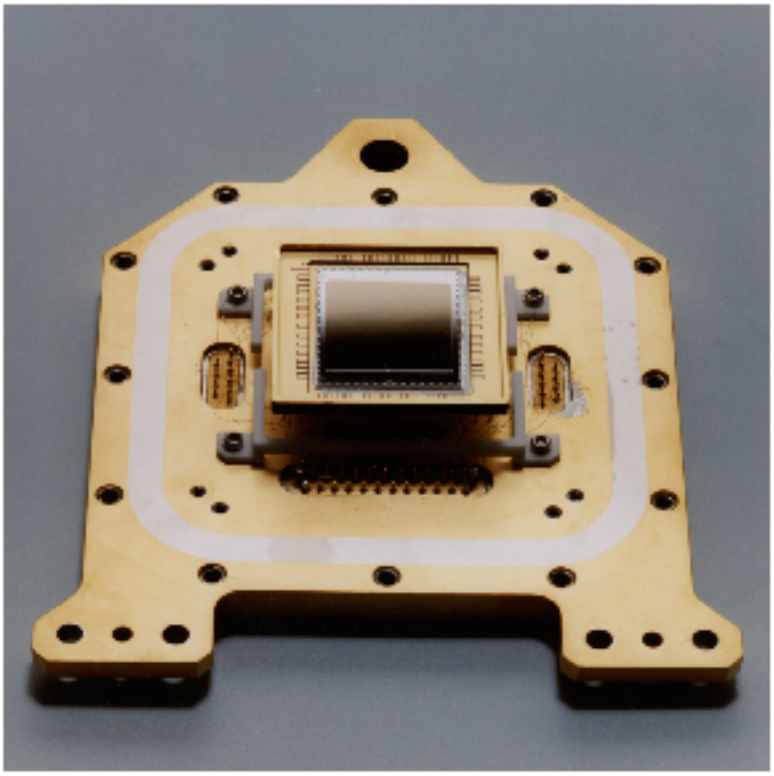

Figure 2: The STIS CCD Detector and Baseplate Mounting Configuration

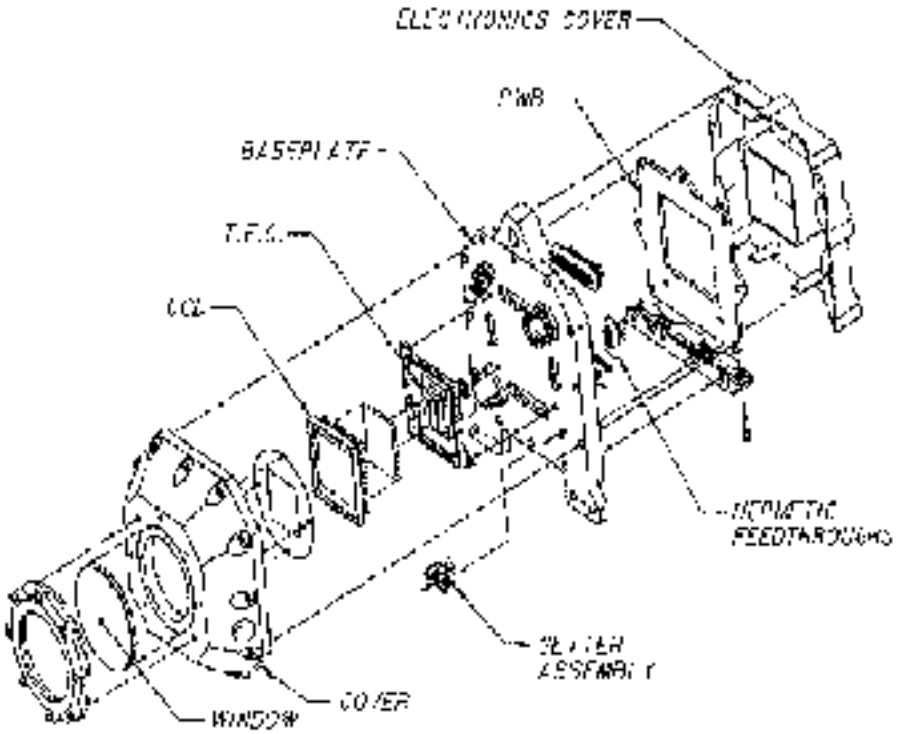

Figure 3: CCD Housing Construction

3. IN-FLIGHT PERFORMANCE

3.1. CCD

The UV enhanced CCD QE (Figure 4) is stable, and does not show QE hysteresis. Figure 4 also illustrates how each of the longer wavelength detectors are capable of providing redundancy for the next shorter wavelength band. Redundancy for the CCD itself is provided by design and operations considerations. The CCD is equipped with four output amplifiers, each of which was tested and functioned normally in initial on-orbit testing. Observations since that initial performance verification have been conducted with the lowest noise amplifier exclusively. The STIS flight software supports full-frame, on-chip binned or subarray readout with any of the four amplifiers as well as two and four amplifier readout modes.[5]

Four commandable gain settings are available for the CCD. The two recommended gain settings are gain = 1 for faint sources where low read noise performance is critical, and gain=4 to utilize the full dynamic range of the CCD. The in-flight noise performance and dynamic range is tabulated in Table 1. The in-flight values measured for the gain are consistent with the more precise values measured during ground calibration and also presented in Table 1.

At the nominal in-flight operating temperature of -83°C, the median dark current is only $\sim$0.0015e$^-$pixel^{-1}s^{-1} or 5-6 e$^-$pixel^{-1}hour^{-1}. The dark current contribution to the noise is much less than the read noise except for lengthy binned exposures where the contribution from the dark current can be comparable to the read noise.[5]

However, for lengthy exposures the cosmic ray rate of 30-40 pixels s^{-1} (at a level greater than 20e$^-$)[5] becomes formidable. In practice, cosmic rays are removed by specifying CR-SPLIT exposures to obtain multiple images from which cosmic rays can be vetoed.

As expected, energetic particle impacts on the CCD produce "hot pixels" with enhanced dark current. A fraction of these pixels return to their nominal state by warming the CCD. By turning off the thermoelectric cooler, the CCD reaches a temperature of -5°C. Annealing at this temperature for 12 hours is scheduled for each month. Annealing cycles to date show that the net growth rate of hot pixels (>0.2e$^-$ sec^{-1}) is down to about 27% of the instantaneous growth rate. From the WFPC2 experience, this performance is expected to improve as the hot pixel count asymptotically approaches a steady state. When normalized for area, time since launch, and operating

Table 1. CCD Noise/Dynamic Range.

Nominal Gain e/DN	Measured Gain e/DN	Noise (rms) *In-flight data*	Linear Range At 1% Rolloff	Single Frame Dynamic Range = Linear Range/Noise
1	0.995	4.0 DN = 4.0 e	33,000 e	8,250
2	2.01	2.7 DN = 5.4 e	86,000 e	16,000
4	4.11	1.7 DN = 7.0 e	144,000 e	20,600
8	8.38	1.3 DN = 10.9 e	144,000 e	13,200

temperature, the STIS and WFPC2 hot pixel rates are comparable. However, the impact of cosmic rays on science data is greater for STIS because of the larger pixel size and warmer operating temperature of the STIS CCD. In practice, CCD dark frames are taken frequently to flag hot pixels for the benefit of target acquisition and science exposures. Dithering the pointing between obserations to permit hot pixel vetoing is the most effective means of reducing the impact of hot pixels on science data.

CTE measurements were conducted at the component level using x-ray techniques. Using this method, a CTE of 0.999994 at 1620e^- was measured in the parallel direction. The serial CTE is higher. The CTE measured during the ground-based end-to-end calibration of STIS was computed using both edge response and sparse field techniques. The sparse field illumination is similar to the illumination that would be encountered from a point source spectrum or a dilute star field. Ground calibrations using this method implied a charge loss up to 1.1% from the top of the CCD column to the bottom, for signal levels of 500e^- pixel^{-1} operating at the gain=1 voltage settings. For higher signals or the gain=4 voltages, the derived charge loss across the detector is lower.[11] Edge response techniques for measuring the CTE in flight show no significant change[5] from the ground measurement of 0.999991 at 200e^- and 0.99996 at 10e^-. A more representative sparse field illumination test of the CTE will soon be implemented in-flight.

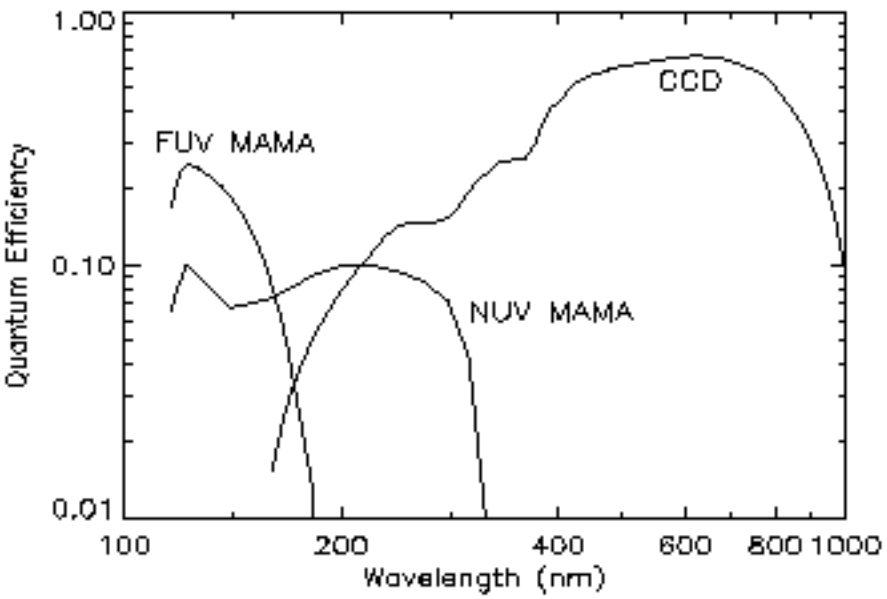

Figure 4: STIS Dectector Quantum Efficiency

Instantanous detector bias levels are determined by fitting both the CCD serial and parallel overscan regions. The parallel fit is offset to match the serial value at each row. The offset parallel fit is then subtracted row by row. A scaled superbias is also constructed and subtracted from the data. Although the mean value of the bias value varies over roughly 10 DN at a gain of 1 and 3 DN at a gain of 4 due to fluctuations in the temperature of the CCD and

Table 2. Key MAMA Performance Parameters

	FUV MAMA	NUV MAMA
Wavelength Range	115 - 170 nm	165-310 prime 115 - 170 backup
Low-res Pixel Size	25 μm × 25 μm	25 μm × 25 μm
Spatial Resolution (FWHM) (w/hi-res readout)	22.7 μm	29.3 μm
Quantum Efficiency	~21% (142 nm)	~9.5% (237 nm)
Dark Rate	5-10 × 10^{-6} cts/pix/s*	0.6-1.5 × 10^{-3} cts/pix/s*
Dynamic Range (10% rolloff)		
Local (MCP limited)	220 cts/pixel/s*	340 cts/pixel/s*
Global (electronics limited)	305,000 cts/s	305,000 cts/s
Flat Field Uniformity (low-res pixels*)	6.4% rms	3.1% rms
Flat Field Stability (changes in 2x2 pixels*)	over 4 months <1% rms	over 21 days <0.68% rms
Visible Light Rejection (QE at 400 nm)	$1.5x10^{-10}$	$2.7x10^{-4}$

the processing electronics, the shape of the bias frames is constant to within <0.2 DN.[5] Consequently, fits to the overscan regions are effective in removing the detector bias level.

While the SITe UV enhanced, backside illuminated, CCD exhibits increased QE in the ultraviolet, an unpleasant feature of the device at long wavelengths was discovered late in the ground calibration. There is a significant degradation of the CCD point spread function (PSF) at wavelengths longer than ~750 nm.[11] While the PSF core remains sharp there is a significant halo observed in the regime where silicon becomes more transparent. This halo results from the fraction of incident light that reaches and then scatters within the translucent substrate material in the backside illuminated device. The halo diameter increases with increasing wavelength; however the fraction of light in each halo pixel is small, thus the slit extraction height is not increased to accomodate the CCD PSF at longer wavelengths. To do so would compromise the spectral purity of the extracted spectrum for a small increase in signal.

From ground calibration the CCD pixel-to-pixel stability is better than 0.1% rms over several hours. Performance was measured at multiple wavelengths spannning the CCD format. In-flight, broad-band, flat-field exposures spanning a month indicate that the flat field stability is <0.2% rms. At longer wavelengths, where the silicon becomes increasingly transparent, interference between the incident light and light reflected by the substrate creates a fringing pattern which must be removed. At wavelengths longward of ~750 nm fringing is an issue. The peak-to-peak amplitude measured at 980 nm is 25% in mode G6750L. In mode G750M, where the higher dispersion creates a more monochromatic beam which exacerbates the fringing, the peak-to-peak fringe amplitude is 32%. Due to grating non-repeatability, typically 2 pixels, and thermal drifts[12] the fringe pattern is not stable in time and requires the acquisition of contemporaneous flats. These flats can be acquired using the on-board tungsten lamp during target occultation. By appropriately structuring the observing proposal, contemporaneous fringe flats can usually be acquired with no time penalty to the observer.

The spatial extent of the source along the slit is also an issue in fringe removal. For extended sources, but not point sources, the CCD PSF halo creates a smooth pedestal beneath the fringe modulation. Thus, point source and extended source spectra have different flat field acquisition requirements. To date fringes have been removed to better than 1% to ~950 nm for a WD spectrum using a short slit flat and for the extended source, Io, using a long slit flat.[13] At longer wavelengths, STIS visible imaging is acquired with the broad band long pass filter. Consequently fringing should not be an issue unless the source is a long wavelength, monochromatic, emission line source.

3.2. MAMA

Key performance parameters for the STIS ultraviolet imaging MAMA detectors are presented in Table 2 (*note: the pixels referred to in the table are low resolution pixels). With the exception of the dark rate, the parameters tabulated are from ground measurements. In flight performance for the detector only PSF and quantum efficiencey cannot be measured directly. However, end-to-end system performance[15,14] indicates that the detectors are operating nominally.

The close agreement between the dark rate measured on the ground and the in-flight dark rate of the FUV MAMA confirms the successful rejection of Cherenkov events produced in the detector window. Cherenkov photons, produced by a particle transit through the detector window, are effectively simultaneous and hence rejected by the MAMA event processing logic. This radiation was the dominant background fro the first genereation HST Digicon detectors employed by GHRS and FOS.

While the FUV MAMA background is a positive achievement at 5-10 times lower than specification, the NUV MAMA background is a disappointment and an order of magnitude higher than specification. Ground tests were conducted on the MAMA detector windows to examine them for impurities in the windows which could be excited to metastable states by energetic particles. Phosphorescent de-excitation of these states procuces UV photons that would then be detected by the MAMA photocathode. Unfortunately, an error in early testing passed the boule from which the NUV MAMA window was fabricated. Over a typical 2000s single exposure, the resulting dark count signal in a standard 2×11 pixel spectral extraction slit is 30-70 counts. Use of a smaller extraction slit can further reduce the dark level. The impact of the elevated dark rate is most severe for long programs or those with very low signal-to-noise, especially those which require binning of the data.[5]

Given the limited heritage, especially over large temporal baselines, of the MAMA detectors and the excellent stability of the GHRS Digicon detector, there has been concern over the signal-to-noise achievable using the MAMA detectors. In-flight measurements, using limited data from orbital verification programs, indicates that a signal-to-noise of $\sim$130 per spectral resolution element can be achieved from a single point source observation with the FUV MAMA and $\sim$150 per spectral resolution element for the NUV MAMA.[3,4] When observing in the echelle modes, on-board Doppler compensation smooths the detector responsivity. In this case, a S/N of $\sim$250 in the FUV and $\sim$350 in the NUV[3] per spectral resolution element have been achieved by acquiring multiple spectra with the fixed pattern (FP) split slits which further smooth the detector responsivity by displacing the individual spectra solely in the spectral direction. These important results are discussed more fully in the following sections.

It should also be noted that operations of STIS have been impacted by the radiation environment in space. To minimize electronic noise STIS employs optical-isolators between the STIS control section microprocessor and MAMA and CCD control electronics. Unfortunately, the detector reset circuitry has been found to respond to transient spikes on the outputs of the optical-isolator components by partially resetting the detectors. In the CCD subsystem the partial resets are relatively infrequent, roughly one per month of continuous operation, and are benign. Consequently, by configuring the CCD voltages at each SAA exit or before CCD observation blocks, the chances of losing data from a CCD reset are negligible. In the MAMA subsystem resets can be more frequent and more complex. To alleviate stresses and risk in the MAMA subsystem, the MAMA low voltage is cycled off for each SAA passage. Otherwise the MAMA low voltage is on to maintain thermal stability.[12] The MAMA high voltage is ramped up and down once per day for the contiguous block of non-SAA-crossing orbits, if the MAMA is scheduled for use that day. This lowers the available duty cycles for MAMA observations to about 40% of HST orbits. After approximately 8 months of operation with MAMA operation forbidden within a defined set of SAA contours, the contours were relaxed slightly. Operation with the relaxed contour set is currently being evaluated. A more complete discussion of the opto-isolator's impact on STIS operations can be found in Kimble et al.[5]

4. ULTRAVIOLET FLAT FIELD CONSTRUCTION AND EVALUATION

From the SMOV program executed during the first six months after the installation of STIS in HST, a handful of data sets emerged which were capable of, or had been designed to test the signal-to-noise capability of STIS in the ultraviolet. These data sets place a lower limit on the UV signal-to-noise capability of STIS. The existing data sets are constrained by the counting statistics in the stellar spectrum for both the low resolution and echelle modes; the co-added low resolution FUV spectra of GRW+70D58 may be limited by the composition of the FUV flat field at a signal-to-noise of $\gtrsim$180 per spectral resolution element.

Concern regarding the capability of STIS to acquire high signal-to-noise spectra was motivated by the lack of heritage for the MAMA detectors in high signal-to-noise astronomical applications, the success of STIS's predecessor (GHRS) in obtaining high signal-to-noise spectra, and the difficulty in obtaining large area UV flat fields. Furthermore, the large number of STIS optical modes and the limited lifetime of the on-board UV continuum lamps necessitated the acquisition of flats at a limited number of central wavelengths spanning the spectral format. These flats would then be applied to both high and low resolution modes.

Given the limited heritage of the MAMA detectors prior to the ground-based science calibration of STIS, the wavelength dependence of the flat fields was unknown. The different STIS optical modes illuminate the appropriate MAMA detector over a range of angles. Angle of incidence effects, resulting from locating the FUV photocathode directly on the MCP far from the detector window and its metallic layer (whose transmission may not be perfectly uniform) were also unknown - and a concern.

Contemporaneous analysis of the NUV flat fields acquired with both internal and external lamps during ground-based science calibration verified that the NUV flat fields were neither wavelength nor mode dependent. In addition, deep exposures with the internal deuterium lamp at a single central wavelength (λ2659) confirmed that the flat field was stable (at a S/N of 100:1 per pixel) over a 21 day baseline. The NUV flat field currently in the pipeline consists solely of this ground-based data set. It is this flat was used to evaluate the S/N of the post-launch NUV spectra.

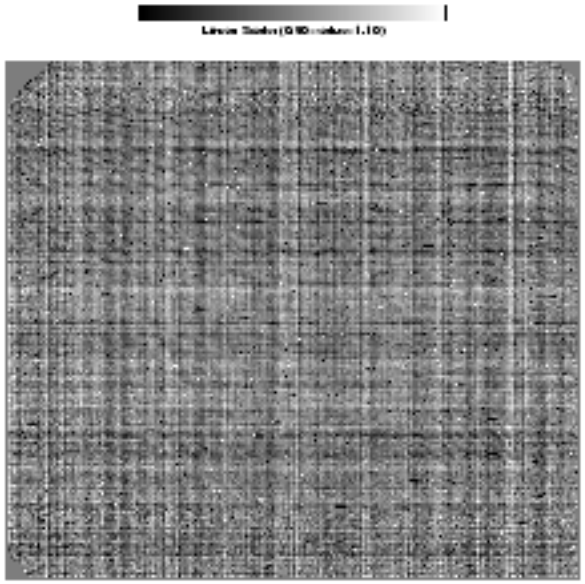

Figure 5: Combined NUV Flat Field

Analysis of the FUV flats indicates they are also wavelength independent. As a result, this discussion of the FUV flat field will focus on the potential optical mode dependence of the flat field which drove the FUV flat field acquisition program. Initial flats acquired with the external lamps in the medium resolution modes showed mode dependencies that were probably due, in part, to the poor spatial illumination of the detector with the long slit flats. This motivated a change in the acquisition strategy for the FUV flat fields. It was still necessary to acquire the flats using external sources, if possible, due to the limited lifetime of the internal krypton lamp. Lamp lifetime is limited by the rate of photopolymerization of contaminants onto the lamp window, a process which is accelerated at shorter wavelengths. Consequently the ground-based FUV flats were acquired in the echelle modes where the demand for high signal-to-noise spectroscopy would be greatest. The inter-order separations were illuminated by tilting the cross-dispersion grating by a small amount corresponding to 0.5″ on the detector. The ground-based FUV flat was constructed from echelle spectra using external argon, krypton, and xenon lamps to span the spectral format. These echelle flats were combined with an initial set of long-slit first-order low resolution post-launch flats. The post-launch flats were acquired at non-optimal grating settings but were capable of improving the count statistics in the remaining small inter-order gaps in the echelle flats. The construction of the flats is described more fully in Bohlin et al.,[16] and Kaiser et al.[3,4]

Both the NUV and FUV flat fields were evaluated using an image ratio test. For the NUV flat field, images were combined at a given wavelength. Each flat at a given wavelength was evaluated in comparison with the extreme wavelength 2977Å flat with the best statistics. The results are presented in Table 3 where the entries are the one sigma values for ratios of images.

The first set of data presented is for a 512×512 flat field image. This image has been binned to consist of 2×2 pixel resolution elements. The 1024×1024 image is for the nominal low resolution pixel format. The 2048×2048

Table 3. Statistics for the Ratio of NUV Flat Fields to the 2977Å Flat

	1769	1933	2176	2419	2419	2419	2659	2659	2659	2659	2977
Date	9/11/96	9/11/96	8/29/96	8/29/96	9/1/96	11/12/96	8/23/96	8/26/96	8/30/96	9/16/96	9/1/96
P FLATS (512x512)											
Poisson (%)	1.23	1.38	1.33	2.05	1.50	1.99	1.05	1.65	2.09	1.25	2.07
Actual sigma (%)	1.24	1.41	1.33	2.04	1.50	2.02	1.07	1.64	2.07	1.33	2.06
Resid. sigma (%)	0.20	0.27	0.00	0.00	0.02	0.38	0.19	0.00	0.00	0.46	0.00
P FLATS (1024x1024)											
Poisson (%)	2.45	2.77	2.67	4.09	2.99	3.98	2.10	3.29	4.18	2.50	4.14
Actual sigma (%)	2.47	2.80	2.67	4.02	2.99	4.01	2.12	3.31	4.17	2.63	4.13
Resid. sigma (%)	0.29	0.42	0.12	0.00	0.11	0.56	0.34	0.31	0.00	0.80	0.00
P FLATS (2048x2048)											
Poisson (%)	4.91	5.53	5.33	8.18	5.98	7.95	4.19	6.59	8.35	5.00	8.28
Actual sigma (%)	5.72	6.47	6.15	8.96	6.89	12.18	4.87	7.25	9.63	11.01	9.55
Resid. sigma (%)	2.95	3.34	3.05	3.66	3.42	9.22	2.48	3.04	4.79	9.81	4.75

image is in the high resolution format whereby the processing electronics centriod event positions to half the spacing of the anode array providing improved sampling and higher resolution[17] at the expense of greater flat field variations as is indicated in the table.

The first row for each of the three image sizes is the expected sigma from counting statistics, the second row is the actual scatter in the ratio images, and the third row measures the actual difference between the two ratioed images. In other words, the third row of each set reflects the actual scatter with the Poisson uncertainty removed in quadrature. The results are consistent with no wavelength dependence and little MAMA contribution to the scatter per low-res pixel or per resolution element. There is a residual scatter of a few percent in the high-res ratios, which demonstrates the nearly complete removal of the large 60% pixel-to-pixel variation of the high-res flats. Since the tabulated Poisson statistics utilize the average counts, the Poisson entries for the high-res case are underestimates of sigma because of the large change in sensitivity between adjacent pixels due to the odd-even effect in the MAMA electronics. The corresponding high-res residuals are overestimates.

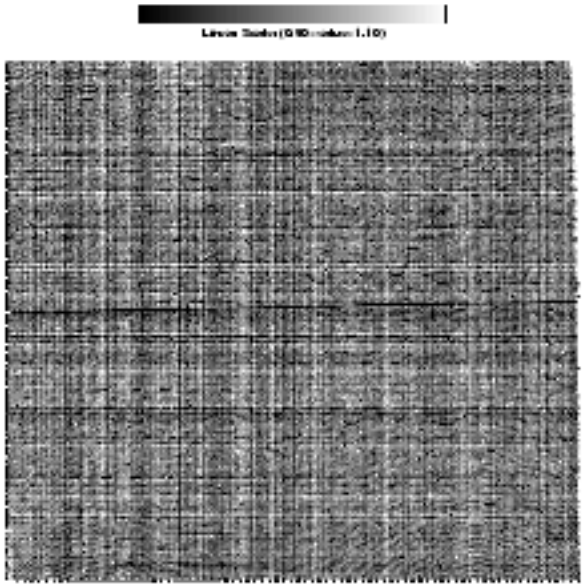

Figure 6: Combined FUV Flat Field

Flat field illumination with the external deuterium lamp does not completely fill the slit at the shortest wavelengths of 1769Å and 1933Å. Consequently, these images were only used for completeness in testing the wavelength independence of the flat field. The NUV superflat is the combination of the data at the G230M central wavelengths

Table 4. Statistics for the Ratio of the FUV G140L Flat Field to the Flats from Other Modes

	G140M	E140M	E140H
P FLATS (512x512)			
Poisson (%)	1.61	1.10	0.75
Actual sigma (%)	2.02	1.72	1.37
Resid. sigma (%)	1.20	1.32	1.15
P FLATS (1024x1024)			
Poisson (%)	3.23	2.20	1.49
Actual sigma (%)	4.02	3.16	2.47
Resid. sigma (%)	2.39	2.27	1.96
P FLATS (2048x2048)			
Poisson (%)	7.14	5.16	3.63
Actual sigma (%)	11.23	11.65	9.07
Resid. sigma (%)	8.67	10.45	8.31

of 2176, 2419, 2659, and 2977A and is shown in Figure 5. Note, the upper and lower left-hand corners of the image are masked slightly by a baffle at the window of the NUV MAMA. The Poisson statistic of 0.30% per resolution element for the superflat correspond to a S/N=333 in regions without fiducial or slit defect masks.

For the FUV flat, images at each central wavelength for a specific optical mode were combined and evaluated, through an image ratio test, with the other flats in the same mode. No wavelength dependence was observed. Then these superflats for each mode were evaluated with respect to the mode G140L superflat using an image ratio test analogous to the NUV evaluation. The results are tabulated in Table 4. From the third row for each of the three image sizes, we note that the residuals do not differ dramatically between optical modes. Calculating the residuals for an extracted spectral resolution element (2×11 pixels) yields residuals of 0.97%, 0.92%, and 0.80% for the ratio of the G140L flat to the G140M, E140M, and E140H flat fields, respectively. There is some residual scatter which may limit the achievable signal-to-noise for some high signal-to-noise, low resolution, programs which do not employ additional techniques such as dithering or FP split slits to further reduce the high frequency flat field variations. It should also be noted that for the echelle flats the image ratio is testing the pre-launch to post-launch residual as well. The combined FUV superflat has a Poisson derived S/N >500 per resolution element for the central columns of the detector not subject to masks or small residual inter-order gaps. At the detector edges the S/N decreases to $\gtrsim$150 per resolution element.

From a visual inspection of the flat field images it is apparent that there is a residual effect in removing an overall moire pattern from the FUV flat field. The amplitude of the residual moire pattern is $\lesssim 6\%$ peak-to-peak. The pattern is visible in both the NUV (Figure 5) and FUV (Figure 6) flats, but it is more pronounced in the FUV flat field. A more complete discussion of the FUV flat field evaluation can be found in Kaiser et al.[3]

5. SIGNAL-TO-NOISE

The signal-to-noise was evaluated for three separate cases, a single spectrum of a point source, multiple spectra of a point source, and spectra acquired using a fixed pattern (FP) split slit whereby spectra are acquired at the same spatial location but are shifted spectrally on the detector. It is important to distinguish between these cases due to the additional smoothing provided by coaddition of non-coincident spectra.

In practice, the IDT calibration pipeline employs a spectral extraction height of 11 pixels in the spatial direction and the spectral resolution is nominally two pixels. Therefore the S/N quoted for a point source, as defined in this paper, is per spectral resolution element (11×2 pixels) unless noted otherwise. This extraction height encompasses 60% - 80% of the energy, depending upon the optical mode and wavelength. However, the signal-to-noise specification is per resolution element, implying a 2×2 low-resolution element. The relative transmission of these spatial extraction heights in the FUV are $\sim$45% at 1423Å for mode G140L and $\sim$56% at 1367Å for E140M. In the NUV the relative extraction height throughputs are $\sim$60% at 2371Å for G230L and $\sim$69% at 2616Å for E230M.

Table 5. NUV Signal-to-Noise Capabilities for a G230L Point Source Spectrum

Star	Spectral Class (B Mag)	Exposure Time	Flat Composition	Spectral Range	S/N (Counting Statistics)	S/N
GRW+70D58	DA3 (12.63)	636.0	NO Flat	1698 - 2167	<165>	<100>
				2167 - 2520	<204>	<101>
				2520 - 3050	<163>	<102>
			G230M	1698 - 2167	<165>	<154>
				2167 - 2520	<204>	<149>
				2520 - 3050	<163>	<152>

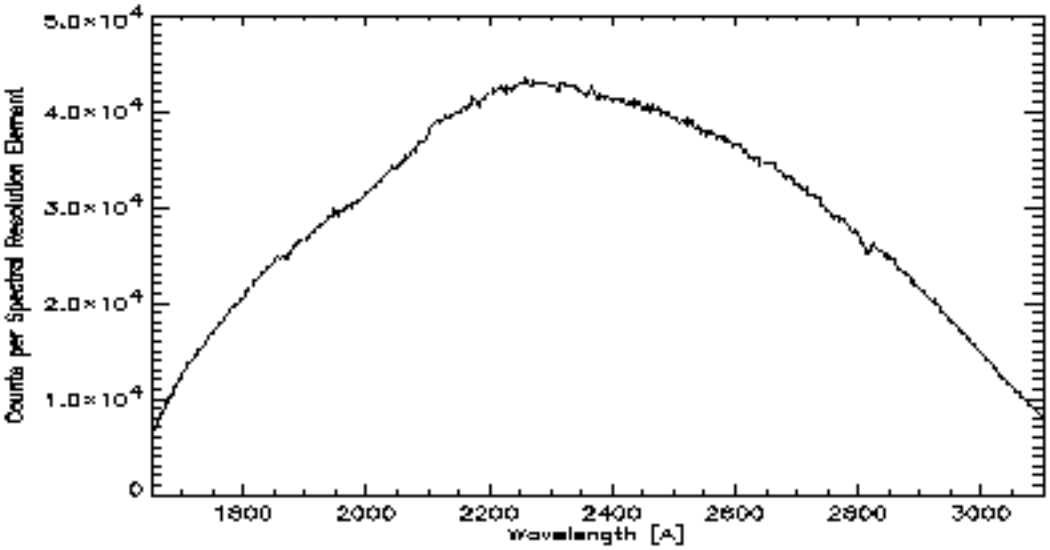

Figure 7: NUV Flat Fielded Spectrum of GRW+70D58

For the case of a single point source spectrum, spectra of GRW+70D58 in mode G230L (Figure 7) and GD153 in mode G140L were flat fielded to determine the realizable S/N. Initially the data is background subtracted, then extracted, and binned in the spectral direction. The 1-D spectrum is then partitioned into segments composed of 20 bins each which are fit with a three-node spline. A three-node spline was used because it provided a good fit to the data without being too sensitive to small scale fluctuations in the data. Consistent results were obtained with fits performed using 15-30 bins per segment. Twenty bin segments were fit, in general, because they provide enough bins for a robust fit while minimizing the number of segments impacted by spectral features. Each segment is divided by its fit; the mean and standard deviation are calculated and ratioed to determine the S/N for each segment. The average of the S/N over the spectral segments contained within the specified spectral range is tabulated in Table 5 for the NUV and Table 6 for the FUV. For the NUV MAMA, the GRW+70D58 spectrum has a peak potential S/N, corresponding to pure counting statistics, of ∼200 per spectral resolution element. The realized S/N is ∼105 *without the application of a flat field* and ∼150 after application of the NUV flat field. For the FUV MAMA, the GD153 spectrum has a peak potential S/N, corresponding to pure counting statistics, of ∼165 per spectral resolution element. The realized S/N is ∼85 *without the application of a flat field* and ∼130 after application of the FUV flat field.

To further test the S/N limit in the FUV, six G140L spectra of GRW+70D58 (Figure 8) were coadded. No shifts were applied to align the spectra. Over the region extending from 1347-1502Å the S/N of the composite spectrum is ∼180, with S/N ∼300 from pure counting statistics. It should be cautioned however that these spectra are neither spatially nor spectrally coincident, exhibiting an offset of ∼10 pixels spectrally and ∼4 pixels spatially. Consequently a single spectrum of comparable count statistics may yield a slightly lower S/N. These results are also presented in Table 6. For the FUV spectral range extending from 1502Å through 1657Å, in both GD153 and GRW+70D58, the counting statistics are poorer thus limiting the signal-to-noise.

Table 6. FUV Signal-to-Noise Capabilities for a G140L Point Source Spectrum

Star	Spectral Class (B Mag)	Exposure Time	Flat Composition	Spectral Range	S/N (Counting Statistics)	S/N
GD153	DA1 (13.07)	187.1	NO Flat	1280 - 1458	<165>	<85>
				1502 - 1657	<75>	<65>
			G140L	1280 - 1458	<165>	<113>
				1502 - 1657	<75>	<50>
			G140L + G140M	1280 - 1458	<165>	<116>
				1502 - 1657	<75>	<73>
			E140M + E140H	1280 - 1458	<165>	<127>
				1502 - 1657	<75>	<74>
			G140L + G140M + E140M + E140H	1280 - 1458	<165>	<128>
				1502 - 1657	<75>	<75>
GRW+70D58	DA3 (12.63)	1260.0	NO Flat	1347 - 1502	<295>	<93>
				1502 - 1657	<172>	<81>
			G140L	1347 - 1502	<295>	<184>
				1502 - 1657	<172>	<92>
			G140L + G140M	1347 - 1502	<295>	<189>
				1502 - 1657	<172>	<130>
			E140M + E140H	1347 - 1502	<295>	<168>
				1502 - 1657	<172>	<150>
			G140L + G140M + E140M + E140H	1347 - 1502	<295>	<182>
				1502 - 1657	<172>	<155>

Further inspection of the results indicates that at S/N ~180 the composition of the flat may become important. To achieve a S/N in excess of this, it may be required to use a flat composed solely from the same mode as the observations to eliminate residual angle of incidence effects in the flat. Or, spectra acquired using the FP split slits may be required. It is also possible that the pre-launch data (E140M and E140H) does not flatten the observations as well as the post-launch flats. A program to acquire FUV and NUV flats using the internal UV calibration lamps at optimal grating/wavelength/slit combinations is scheduled for execution within the next several weeks.

Because it was not known whether the ground flats would be valid post-launch, and acquisition of post-launch flats would require a significant investment of time with the valuable limited calibration lamp resource, a proposal was executed to acquire a data set which could be iteratively solved for both the stellar spectrum and the flat field simultaneously. Consequently, exposures were kept short to minimize the impact of Doppler compensation on each individual spectrum. With this technique, exposures are executed using a special set of five, FP split, apertures which offset the spectrum by incommensurate amounts in a purely spectral direction on the detector. This data set was analyzed using both the iterative technique and by employing the ground-based flats. The results obtained from each of these methods are consistent in both the NUV and FUV.

Multiple spectra of BD28D4211 were acquired in the medium resolution echelle modes, E140M and E230M, to test the signal-to-noise capabilities of the STIS MAMA detectors. These data sets were subject to two forms of smoothing. The first form of smoothing arises from the on-board Doppler compensation. In these modes the maximum on-board Doppler compensation is ±3.2 high-res pixels. For the observations of BD28D42 the maximum Doppler compensation was ±3 high-res pixels. Consequently the detector responsitivity is smoothed by ±3 high-res pixels during the integration. The second form of smoothing arises from the design of the FP split slits. These five slits are offset solely in the spectral direction. Therefore the detector responsivity is smoothed when the spectra are shifted, by integral pixels, for coaddition. For this test, only integral pixel shifts were permitted so that interpolation effects would not improve the signal-to-noise.

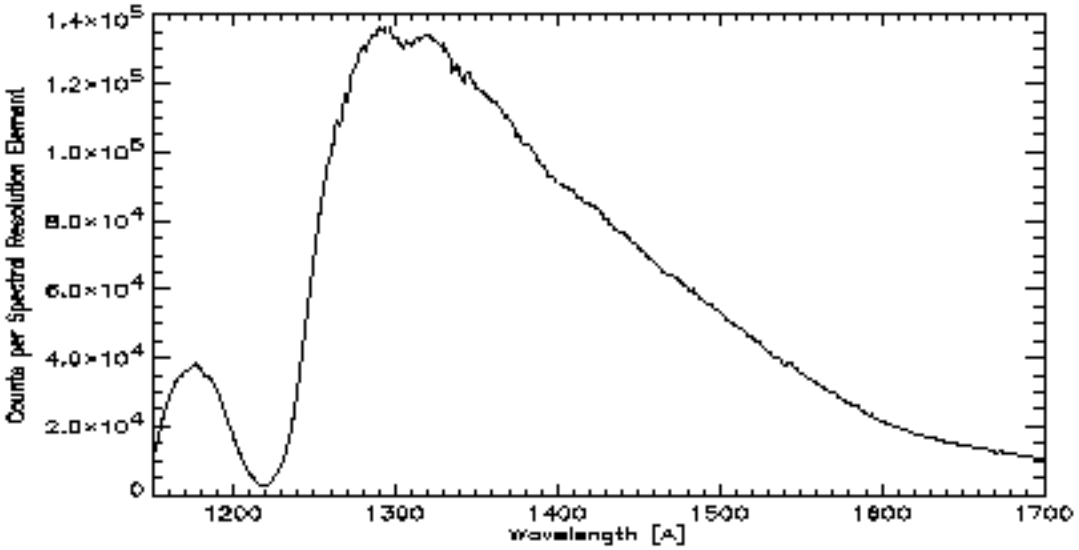

Figure 8: FUV Flat Fielded Combined Spectra of GRW+70D58

For the standard analysis each spectrum was first background subtracted. Next, the flat field was smoothed by the same amount as the on-board Dopppler compensation for that image. Then the doppler smoothed flat was applied to the stellar spectrum. As with the first order modes, an 11 pixel extraction height was used to extract the spectra. The spectra were then binned by 2 in the spectral direction. Each spectral order was partitioned into segments comprised of 20 bins each. Each segment was then divided by a three-node spline-fit to the data. Given the high resolution of the data it was sometimes difficult to distinguish between weak absorption features and variations in the continuum that could be instrumental in origin. Consequently, the spectral regions identified for assessing the S/N represent the highest S/N regions of the spectra. They are potentially biased toward high S/N, whereas in the first order modes the S/N quoted reflects an average S/N about the peak of the counting statistics.

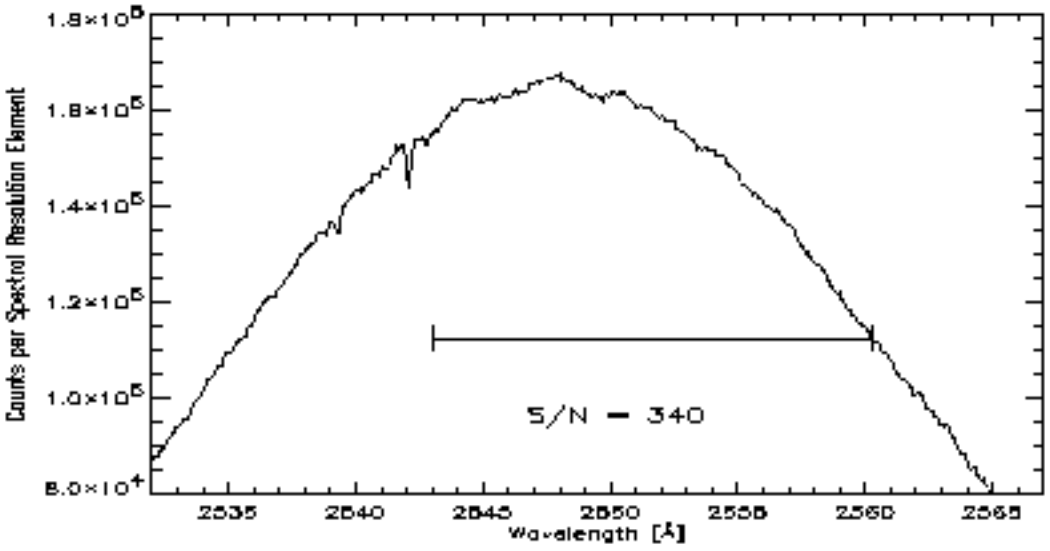

Figure 9: NUV Flat Fielded Echelle Spectra of BD28D4211

The S/N achieved using echelle (Doppler compensated) spectra with the FP split slits and the pipeline flats, is 250 in the FUV and 350 in the NUV. Recall, this result is biased against flat field systematic errors resembling weak absorption features. In the FUV there are numerous stellar features at this resolving power, therefore the signal-to-noise quoted reflects an average calculated for multiple regions of featureless continuum in several orders.

It should be noted that without using any flat at all, the same spectral regions yield a S/N of 200 in the FUV and 290 in the NUV. The counting statistics for these regions are 285 in the FUV and 385 in the NUV.

Figures 9 and 10 illustrate the quality of spectra obtained using the FP split slits. Both figures represent a single order with high counting statistics. The NUV spectrum (Figure 9) is devoid of spectral features, whereas the Figure 10 has numerous spectral features as do the other spectral orders for BD28D4211 in the FUV. The average signal-to-noise for the regions designated on the plots is 340 in the NUV and 280 in the FUV.

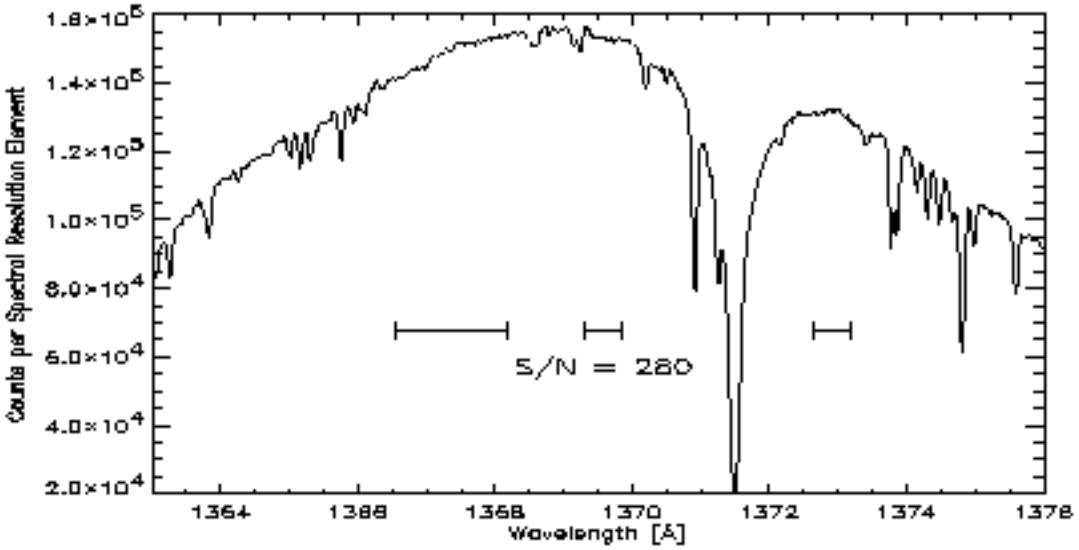

Figure 10: FUV Flat Fielded Echelle Spectra of BD28D4211

The FP split slit observations of BD28D42 were also analyzed using an iterative technique which permits solving the data for both the target spectrum and the flat field response of the instrument. Analysis of the STIS data with the iterative method[18] indicates that a S/N of >250 per low resolution pixel and >350 per spectral resolution element can be acheived in modes E140M and E230M by employing this technique. This is consistent with the results using the pipeline flat and the shift-and-add method for combining the flats in the NUV.

Given the consistency of the results when reducing the FP split slit data by the aforementioned techniques, it is advantageous to employ the pipeline flat rather than solve iteratively for the flat from the stellar spectrum. The advantage lies in the duty cycle for acquiring the spectra. The iterative method relies upon the individual spectra being unadulterated by Doppler compensation. This requires relatively short exposures for targets with declinations $\pm 30^{\circ}$ of the declination of the HST. For the high resolution echelle modes these exposures become prohibitively short, with the orbital visibility period dominated by detector readouts. There is no Doppler smoothing constraint imposed when using the pipeline flat. Consequently, the time required to achieve the required counting statistics is less.

Simulations of the high resolution echelle modes E140H and E230H indicate that the Doppler compensation, up to 12 high-resolution pixels, effectively smooths the detector responsivity sufficiently to acheive a signal-to-noise per resolution element of 330 in the NUV and 140 (without a flat) in the FUV assuming a typical Dompler amplitude of ± 8 high-resolution pixels. Given that the aforementioned FUV spectra of BD28D42 realized a S/N$\sim$200 *without a flat*, using the FP slit slits should further increase the S/N performance over the simulated projected S/N values which only include smoothing the detector responsivity through Doppler compensation.

6. CONCLUSION

STIS is a versatile imaging spectrograph capable of providing spatially extended wavelength coverage from the far ultraviolet (115 nm) to the near-infrared (1 μm). Spectrograph versatility, provided by the large complement of slit/grating/detector combinations, relies upon STIS's two dimensional detectors in both the ultraviolet and the visible. In the year since launch, STIS has performed well. Its UV MAMA detectors have been stable. No detector based sensitivity losses have been observed. Both long slit low resolution first order spectra and medium resolution

echelle spectra illustrate that STIS is capable of achieving a signal-to-noise well exceeding 100:1 per spectral resolution element in the NUV and FUV. A single point source low resolution spectrum of GRW+70D58 in the NUV has a S/N of ∼150 per spectral resolution element. In the FUV, a single point source spectrum of GD153 has a S/N of ∼130 per spectral resolution element. The realized S/N is probably limited by counting statistics in the stellar spectrum for both observations. Co-adding spectra in the FUV achieves a S/N ∼180 which is probably limited by either the optical mode content or pre to post-launch shifts in the flat. Even higher S/N capabilities have been demonstrated through the use of the FP split slits in the Doppler compensated, medium resolution echelle modes where co-added BD28D42 spectra exhibit a S/N of ∼250 in the FUV and ∼350 in the NUV per spectral resolution element.

ACKNOWLEDGMENTS

Realizing an instrument as richly diverse as STIS requires the dedicated efforts of many individuals over several years. We have tried to acknowledge the principal science and engineering participants in the STIS papers[15,12,3,5] presented by the STIS IDT at this conference. Our thanks to all those, named and nameless, who have enabled this instrument to achieve its excellent performance. The STIS IDT has been funded in response to NASA Announcement of Opportunity OSSA-4-84.

REFERENCES

1. B. E. Woodgate et al., "The Space Telescope Imaging Spectrograph (STIS) Design " *PASP*, submitted, 1998.
2. *WFPC2 Instrument Handbook*, STScI, Baltimore, 1996
3. M. E. Kaiser, R. C Bohlin, D. J. Lindler, R. Gilliland, and V. Argabright, "Ultraviolet Signal-to-Noise Capabilities of the Space Telescope Imaging Spectrograph" *PASP*, submitted, 1998.
4. M. E. Kaiser, D. J. Lindler, and R. C Bohlin, "The Flat Fielding and Achievable Signal-to-noise of the MAMA Detectors", *The 1997 HST Calibration Workshop*, eds. S. Casertano, R. Jedrzejewski, T. Keyes, & M. Stevens (Baltimore: STScI), 29, 1997.
5. R. A. Kimble et al., "The On-Orbit Performance of the Space Telescope Imaging Spectrograph", *ApJ*, **492** L83 1998
6. R. A. Kimble et al., "CCD detector for the Space Telescope Imaging Spectrograph", *Ultraviolet Technology V*, Proc SPIE **2282**, 169, 1994.
7. J. G. Timothy, J. S. Morgan, D. C. Slater, D. B. Kasle, R. L. Bybee, and H. E. Culver, "MAMA detector systems: a status report", *Ultraviolet Technology III*, Proc. SPIE **1158**, 104, 1989
8. C. J. Joseph, V. Argabright, R. Bybee, A. Danks and B. Woodgate, "Test and evaluation of the STIS engineering model units of the MAMA detectors" *Ultraviolet Technology V*, Proc. SPIE **2282**, 116, 1994
9. J. Janesick, G. Soli, T. Elliott, and S. Collins, "The effect of proton damage on charg-coupled devices", in *Charge-Coupled Devices and Solid State Optical Sensors II*, Proc SPIE **1447**, , 1991.
10. C. Dale, and P. Marshall, "Displacement damage in Si imagers for space applications", in *Charge-Coupled Devices and Solid State Optical Sensors II*, Proc SPIE **1447**, , 1991.
11. R. A. Kimble, "The on-orbit performance of the STIS detectors", *The 1997 HST Calibration Workshop*, eds. S. Casertano, R. Jedrzejewski, T. Keyes, & M. Stevens (Baltimore: STScI), 1997.
12. T. R. Gull et al., "STIS on-orbit testing: limiting magnitudes, spectral sensitivity, thermal flexure and MAMA time tagging", *Space Telescopes and Instruments V*, Proc SPIE **3356**, this volume, 1998.
13. P. Goudfrooij,J. R. Walsh, and S. A. Baum,"STIS near-IR long slit spectra: fringe correction", *The 1997 HST Calibration Workshop*, eds. S. Casertano, R. Jedrzejewski, T. Keyes, & M. Stevens (Baltimore: STScI), 1997.
14. C. W. Bowers, "The On-Orbit Performance of the STIS", *The 1997 HST Calibration Workshop*, eds. S. Casertano, R. Jedrzejewski, T. Keyes, & M. Stevens (Baltimore: STScI), 1997.
15. C. W. Bowers et al., "STIS on-orbit optical performance", *Space Telescopes and Instruments V*, Proc SPIE **3356**, this volume, 1998.
16. Bohlin, R. C., Lindler, D. J., Kaiser, M. E., Instrument Science Report **STIS 97-07**, *http* : *//www.stsci.edu/ftp/instrument_news/STIS/isrs/stisisr*, 1997
17. D. B. Kasle and J. S. Morgan, "High resolution decoding of Multi-Anode Microchannel Array detectors", *EUV, X-ray, and Gamma-ray Instrumentation for Astronomy II*, Proc SPIE **1549**, 52, 1991.
18. R. Gilliland et al., Instrument Science Report STIS, in prep., 1998